Ocean mixing beneath Pine Island Glacier Ice Shelf

Satoshi Kimura,[1] Pierre Dutrieux,[2] Adrian Jenkins,[1] Alexander Forryan,[3]

Alberto C. Naveira Garabato,[3] Yvonne Firing,[4]

[1]British Antarctic Survey, Cambridge,

U.K.

[2]Polar Science Center, Applied Physics

Laboratory, University of Washington,

U.S.A.

[3]University of Southampton,

Southampton, U.K.

[4]National Oceanography Centre,

Southampton, U.K.

Key Points.

(Type in Key Points Here)

Abstract. Ice shelves around Antarctica are vulnerable to increase in ocean-driven melting, with the melt rate depending on ocean temperature and strength of sub-ice-shelf-cavity circulations. We present repeated measurements of velocity, temperature, salinity, turbulent kinetic energy dissipation rate and thermal variance dissipation rate beneath Pine Island Glacier Ice Shelf, Antarctica, collected by CTD, ADCP and turbulence sensors mounted on an Autonomous Underwater Vehicle (AUV). The turbulence quantities measured by the AUV outside the ice-shelf cavity are in good agreement with ship-based measurements. The highest turbulent kinetic energy dissipation rate is found near the grounding line. The highest thermal variance dissipation rate is found when the AUV was ∼0.5 m away from the ice, and the thermal variance dissipation generally increases with decreasing distance between the AUV and ice.

1. Introduction

Thinning of ice shelves reduces the basal and lateral drags of outlet glaciers, thereby changing the ability of ice shelves to buttress the flow of the grounded ice upstream [*Schoof*, 2007]. Many of the rapidly thinning ice shelves are located in the Amundsen Sea embayment in Antarctica [*Pritchard et al.*, 2009]. In particular, Pine Island Glacier (PIG) Ice Shelf has been highlighted as a major drainage pathway of the West Antarctic Ice Sheet [*Shepherd et al.*, 2001]. Over the past few decades, the ice shelf has gone through a dramatic acceleration and thinning [*Joughin et al.*, 2003; *Shepherd et al.*, 2001]. PIG is grounded on the bed that deepens inland of the grounding line, and there are no topographic barriers to halt the retreat once it has been initiated [*Rignot et al.*, 2014]. Ice sheet model simulations suggest that the irreversible retreat is already underway on the ice shelf, largely in response to the steady high ice-shelf thinning rate [*Joughin et al.*, 2014; *Favier et al.*, 2014]. Thinning of PIG Ice Shelf is thought to be driven by variability in the inflow of Circumpolar Deep Water (CDW), a few degrees above in situ freezing point into the PIG Ice Shelf cavity [*Jacobs et al.*, 1996].

Sampling oceanic conditions beneath the ice shelf are necessary to advance our understanding of the connection between the basal melting and oceanic forcing; however, observations are limited by the difficulty in gaining access through the ice shelf itself. Some oceanic measurements have been made beneath PIG Ice Shelf by either drilling a borehole through the ice shelf [*Stanton et al.*, 2013] or sending an Autonomous Underwater Vehicle (AUV) beneath the ice shelf [*Jenkins et al.*, 2010], both of which require a heavy logistical operation.

The measurements through boreholes beneath PIG Ice Shelf revealed a stratified ice-shelf-ocean boundary layer [*Stanton et al.*, 2013]. The boundary layer is forced by the melt-generated buoyancy acting on the sloping base of the ice shelf. While the measurements through boreholes can provide a long term record, the spatial coverage is limited by the locations of the boreholes. AUV survey has a large spatial coverage, but the battery life limits the length of the survey, which spans up to 2 days. The AUV and airborne radar surveys have characterized general aspects of the ice shelf morphology and ocean cavity bathymetry of PIG [*Jenkins et al.*, 2010; *Vaughan et al.*, 2012; *Dutrieux et al.*, 2014a]. A bathymetric survey by the AUV revealed a ridge oriented perpendicular to the ice flow and indicated that the ice was formerly grounded on top of the ridge [*Jenkins et al.*, 2010]. Retreat of the grounding line has since resulted in the formation of a large ocean cavity behind the ridge. This transverse ridge separates the PIG cavity into two gyres and interaction of these gyres modulates the ocean water properties near the grounding line [*De Rydt et al.*, 2014; *Dutrieux et al.*, 2014b].

The ridge presents an obstruction for the CDW intrusion towards the grounding line, and the ocean mixing processes in the gap above the ridge crest can dictate how quickly the replenishment of CDW occurs at the grounding line. Near the ice, the strength of mixing dictates the transport of heat and salt through the ice-shelf-ocean boundary layer. The heat content within the boundary layer controls the basal melting of the ice shelf which in turn changes the seaward flow of the grounded ice upstream. Identifying mixing hot spots inside the ice-shelf cavity thus is of interest to both glaciologists and oceanographers.

We present microstructure measurements taken by the AUV, Autosub3, beneath PIG Ice Shelf. We begin with our procedure for processing microstructure measurements from

the AUV in section 2. Section 3 and 4 describe an overview of ocean mixing along and across the ice flow, respectively. The measurements near the ice and its implications for the ice-shelf melting are discussed in section 5, and conclusions are presented in section 6.

2. Measurements and methods

A self-contained instrument package for turbulence microstructure measurement, Rockland Scientific MicroRider, was mounted in the nose of the AUV. The AUV operated with a mean speed of 1.4 m s^{-1} and completed two missions totalling 92 hours and covering 460 km of track beneath PIG Ice Shelf (Fig. 1). The first mission (track A) took a series of profiles along the ice flow over a transverse ridge in the sea floor, located approximately 20 km from the ice front. The second mission was launched two days after the first mission and followed two separate tracks, B and C (Fig. 1). Track B was aligned in the direction of the ice flow, whereas track C was a transverse direction. Tracks B and C sampled oceanographic conditions near the grounding line: B reached a point approximately 10 km away from the eastern grounding line, and C reached a point 2 km away from the southern parts of the grounding line. The AUV microstructure observation is complemented by shipboard microstructure measurements, which are used to evaluate the quality of the microstructure measurements from the AUV.

2.1. Processing of microstructure data from the AUV

The turbulent kinetic energy dissipation rate, ϵ, is estimated from shear microstructure measurements with a sampling frequency of 512 Hz, assuming the isotropic relation $\epsilon = 7.5\nu\langle {w'_x}^2 \rangle$, where $\nu = 1.83\times10^{-6}$ m^2 s^{-1} is the viscosity of seawater and $\langle {w'_x}^2 \rangle$ is the shear

variance of the velocity perpendicular to the AUV path x. The variance is calculated by integrating a spectrum up to a cutoff wave number. The path of the AUV is maintained within $\pm 20^\circ$ from the horizontal direction to ensure that the shear probe responds linearly to cross-stream velocity fluctuation as described in *Osborn and Crawford* [1980].

The raw shear signals are contaminated by vibrations of the AUV and acoustic devices for communication with the ship. The accelerometer signals from the MicroRider picked up two distinct spikes with periods of 600 s and 0.5 s. The time interval of 600 s is longer than the time record needed to estimate spectra (at least 1 s), so we simply remove this feature of the shear measurements. The periodic spike at 0.5 s is removed by comparing the signal to its low pass filtered signal with a cutoff frequency of 30 Hz. The shear signal was replaced by zero-padding whenever the difference between the raw and low pass filtered signals exceeded one standard deviation. The remaining signal contamination was removed from the shear power spectra by constructing a filter from the accelerometer signals, following the method outlined in *Levine and Lueck* [1999].

The universal spectra are generated by fitting the variance of the measured shear power spectra for 1-s segments of recorded data between the limits 1-25 cpm for dissipations above 1×10^{-8} W kg^{-1} and between 1-12 cpm for dissipations below 1×10^{-8} W kg^{-1}. Within the integration limits, the observed shear spectra compare well with the universal Nasmyth spectrum (Fig. 2). The AUV vibration does not appear to contaminate the shear spectrum in a relatively energetic environment, and the observed shear spectrum is in good agreement with the spectral rolloff of the universal Nasmyth spectrum (Fig. 2a). In contrast, the spectral rolloff is not well captured in a less energetic environment, and

the contamination from AUV motion appears as a spurious peak between 14 and 22 cpm in the shear spectra (Fig. 2b).

The temperature gradient computed from FP07 thermistors mounted on the MicroRider is used to estimate the thermal variance dissipation rate, defined as $\chi_T = 6\kappa_T\langle(\partial T'/\partial x)^2\rangle$, where $\kappa_T = 1.37 \times 10^{-7}$ m^2 s^{-1} is the molecular diffusivity of heat, and $\partial T'/\partial x$ is the temperature gradient along the path of the AUV. The thermistor signal is calibrated against on board CTD measurements by fitting to a second order polynomial. The time rate of change of the temperature is then calculated and converted to the temperature gradient $\partial T'/\partial x$, by dividing by the speed of the AUV. The variance of the thermal gradient is estimated by fitting the Batchelor spectrum [*Batchelor*, 1959] to the observed spectrum.

The individual estimates of ϵ and χ_T from 1-s segments are averaged over 20 s windows to obtain more robust estimates of ϵ and χ_T. These averaged estimates are in good agreement with the shipboard microstructure measurements from the free-falling microstructure instrument, a Rockland Scientific VMP-250 (Figs. 3a,b). The shipboard microstructure measurements were taken within 4 km of the AUV track a few days prior to the deployment of the AUV. The AUV track was 450 m or more below the surface to avoid a potential collision with the calving front of the ice shelf, so the comparison with the shipboard data was only possible over a limited depth range. Despite these limiting factors, 82% of ϵ and 60% of χ_T estimates from the AUV are within the range of shipboard estimates, and there appear to be no biases in the estimates of ϵ and χ_T. In fact, 8% of ϵ and 20% of χ_T estimates are below the shipboard measurements, and 10% of ϵ and 20% of χ_T estimates are above the shipboard measurements. The ϵ estimates from

the AUV are more consistent with the shipboard measurements than the χ_T estimates. This is likely due to the high variability of χ_T. The measurements were taken where the meltwater from the cavity interacts with the ambient ocean water, producing strong temperature gradients. As a result, χ_T fluctuates over roughly 4 orders of magnitude, whereas the fluctuations of ϵ are within ~ 2 orders of magnitude. The fluctuation of ϵ is relatively stable compared with that of χ_T, resulting in better agreement between the non-coincident AUV and shipboard measurements.

3. Observations along the ice flow (Autosub tracks A and B)

The bottom part (depth > 600 m) of the cavity is flooded by CDW, but the warmest CDW does not penetrate over the ridge (Fig. 4a). At the crest of the ridge, modified CDW is in contact with relatively cool and fresh water incorporating meltwater, increasing the horizontal temperature gradient. The region of high density gradient combined with changes in the water column thickness coincides with the region of high shearing motions. The segment with the largest values of χ_T and ϵ ($\chi_T \sim 10^{-5}$ °C^2 s^{-1} and $\epsilon \sim 10^{-7}$ W kg^{-1}) is found between 35 and 36 km away from the ice front near the bottom, where the ridge slopes toward the grounding line (Figs. 4b,c). These χ_T and ϵ are several orders of magnitude higher than the average values outside the cavity (see Figs 3a,b). As the AUV moves away from the ridge, both χ_T and ϵ decrease to the background values and elevate again near the eastern grounding line.

The three major water masses in Pine Island Bay are CDW, Winter Water (WW) and meltwater [*Jacobs et al.*, 2011]. Broadly speaking, the water column in Pine Island Bay consists of cool ($T \sim -1.5$°C), fresh ($S < 34.4$ psu) WW over warm ($T \sim 1$°C), salty ($S > 34.6$ psu) CDW. These two water masses are separated by a pycnocline,

where the T-S properties lie along an approximately straight line between CDW and WW (Fig. 5a). Meanwhile, the temperature and salinity of any water masses generated by melting of glacial ice should lie on a straight line with a typical slope of $\sim$ 2.7 °C PSU^{-1} (the meltwater mixing line) passing through the temperature and salinity of the water mass that is the source water for melting [*Gade*, 1979; *Greisman*, 1979]. In the PIG ice shelf cavity, the source water for melting is largely CDW with some contribution from pycnocline water (Fig. 5a).

The pycnocline water occupies the upper part of the cavity between 0 and 20 km away from the ice front, and ϵ along the meltwater mixing line in this area is equivalent to the open-ocean background level $O(10^{-10})$ W kg^{-1} (Fig. 5b). The warmest CDW in the cavity ($T \sim 1$°C) does not penetrate beyond 28 km away from the ice front, and the T-S properties farther from the ice front are characterized by the mixture of meltwater and thermocline water (Fig. 5c). A cluster of elevated ϵ between 10^{-8} and 10^{-7} W kg^{-1} is found along $\sigma_\theta = 27.65$ kg m^{-3}, located near the seabed over the crest of the ridge, where the thermocline water interacts with the water from the on shore of the ridge (Fig. 5c). Many measurements of ϵ on oceanic flows over a ridge have been made [e.g. *Rudnick et al.*, 2003; *Sheen et al.*, 2014], and our measurements of ϵ are of similar magnitude. As the AUV approaches closer to the eastern grounding line ($>$ 32 km away from the ice front), T-S properties lie along the meltwater mixing line and high ϵ, suggesting vigorous mixing of meltwater near the grounding line (Fig. 5d).

4. Observations across the ice flow (Autosub track C)

The ice base morphology in the direction transverse to the ice flow has channels and steps, and the track C collected data across these structures (Fig. 6). The water column

thickness beneath the ice shelf varies between 120 and 620 m, and the keels between channels are exposed to warmer water (Fig. 6a). The presence of the warm water near the ice implies high temperature gradients and indeed χ_T tends to increase near the keels (Fig. 6b). Elevated bands of $\chi_T \sim 10^{-5}$ °C^2 s^{-1} are found near the ice, where the AUV ascended to approximately 0.5 m away from the ice shelf; ϵ here is $\sim 10^{-9}$ W kg^{-1}, an order of magnitude larger than the background level. The highest ϵ of 1.35×10^{-7} W kg^{-1} is observed approximately 2 km away from the southern grounding line, three orders of magnitude larger than the background ϵ, and an order of magnitude larger than its value at the crest of the ridge (Fig. 6c).

A sharp temperature gradient is maintained within 20 m of the ice shelf (Fig. 7a). During the horizontal track in the vicinity of the ice, the average temperature was -0.41 °C, 1.76 °C above the *in situ* freezing point; the standard deviation was 0.12 °C. The horizontal current speed within 40 m of the ice shelf is relatively slow, 0.07 m s^{-1}, and the speed tends to increase further away from the ice (Fig. 7b). Near the ice, ϵ and χ_T increase up to 6.2×10^{-8} W kg^{-1} and 2×10^{-5} °C^2 s^{-1} (Fig. 7c).

5. Discussion

Oceanic values of ϵ have a wide range, spanning about 10 orders of magnitude from 10^{-11} W kg^{-1} in the abyssal ocean up to 10^{-1} W kg^{-1} in the regions of extremely active mixing, e.g., surf zone and fast tidal zone. There have been no previous measurements to confirm the range of ϵ beneath an ice shelf. Our measurements show that the range of ϵ beneath PIG ice shelf extends from the background value of 10^{-10} W kg^{-1} up to 10^{-7} W kg^{-1}, near the grounding line. The highest ϵ of 1.35×10^{-7} W kg^{-1} was observed 2 km away from the southern grounding line, the closest approach to the grounding line.

5.1. Estimation of u_* from ϵ near the ice

The basal melting of ice shelves due to oceanic forcing is difficult to parameterize. The problem is partly due to our lack of understanding of the turbulent transports within the ice-shelf-ocean boundary layer, and the flow condition beneath ice shelves varies between different ice shelves. Direct oceanographic measurements beneath ice shelves have revealed both high and low Reynolds number regimes. Observations beneath ice shelves, surrounded by water that is near in situ freezing point, such as Filchner-Ronne, Larsen C and Ross ice shelves, suggest that the flow is in the high Reynolds number regime as a result of the large-scale circulation, modulated by tidal motion [*Jacobs et al.*, 1979; *Nicholls and Jenkins*, 1993]. In contrast, distinct signatures of thermohaline staircases (a stack of well-mixed layers separated by sharp interfaces) were seen in the profiles beneath George VI Ice Shelf in the Bellingshausen Sea, Antarctica [*Kimura et al.*, 2015].

The turbulent transport of momentum, heat and salt can be parameterized in term of friction velocity, u_*, associated with the Reynolds stress beneath an ice shelf. A parameterization of u_* is routinely used in general circulation models (GCMs) in order to estimate melt rate of ice shelves [e.g. *Holland and Jenkins*, 2001; *Losch*, 2008; *Holland et al.*, 2008; *Little et al.*, 2009]. Despite widespread interest in understanding how oceanic turbulence distributes momentum, heat and salt at the ice-ocean interface, direct flux measurements within the ice-shelf-ocean boundary layer are rare, mostly due to the difficulty in gaining access through the ice shelf.

The appropriate Reynolds stress is defined by the covariance of horizontal and vertical velocity fluctuations as

$$\tau = -\rho\overline{u'w'}, \tag{1}$$

where u' and w' are the velocity fluctuations [*Tennekes and Lumley*, 1972]. The variable ρ represents the density of seawater. At the ice-ocean interface, the stress exerted by the ice must match the stress in the ocean, so a scale of the velocity fluctuation can be expressed as

$$u_*^2 \sim u'w'. \tag{2}$$

In a steady stratified shear flow, the rate of turbulent kinetic energy production by the Reynolds stress working against the mean shear (shear production) is balanced by the turbulent kinetic energy dissipation rate and buoyancy production term:

$$\frac{\tau}{\rho} \cdot \frac{dU}{dz} = \epsilon - \overline{w'b'}. \tag{3}$$

A non-dimensionalized mean shear ϕ_m can be expressed as

$$\phi_m = \frac{\kappa z}{u_*} \frac{dU}{dz}, \tag{4}$$

where κ and z represent von Kármán's constant and distance from the ice, respectively. Measurements of κ in marine environments are approximately equal to 0.4 [*Soulsby*, 1983]. Several forms of ϕ_m have been suggested. In the absence of the stratification, the mixing length depends only on distance from the ice, z, following the mixing length argument of Prandtl, thereby

$$\phi_m = 1. \tag{5}$$

In this case, integration of (4) yields the law of the wall, which states that the mean velocity of the turbulent flow, $U(z)$, is proportional to the logarithm of the distance from the wall: $U = \frac{u_*}{\kappa} \ln\left(\frac{z}{z_0}\right)$, where z_0 is a constant of integration such that $U(z_0) = 0$ and represents a length scale proportional to the roughness of the ice base.

For a stably stratified boundary layer, *Monin and Obukhov* [1954] argued that ϕ_m is a function of the non-dimensional height $\xi = z/L_o$. The variable L_o is the Obukhov length, defined as

$$L_o = -\frac{u_*^3}{\kappa \overline{w'b'}}. \tag{6}$$

Many studies have empirically determined a form of $\phi_m(\xi)$ for the atmospheric boundary layer. The first order empirical formula for a stably stratified boundary layer is

$$\phi_m(\xi) = 1 + \gamma\xi. \tag{7}$$

Estimates of γ from the atmospheric boundary layer vary widely from 0.6 to near 5 [e.g. *Halstead*, 1943; *Dyer*, 1974; *Businger et al.*, 1971].

Combing the scaling of (2) and (4), the turbulent kinetic energy budget (3) results in an expression for u_* in terms of ϵ and $\overline{w'b'}$: $u_* = \left[\kappa z(\epsilon - (1-\gamma)\overline{w'b'})\right]^{\frac{1}{3}}$. We use two different values of γ, $\gamma = 0$ and $\gamma = 0.6$:

$$u_* = \begin{cases} [\kappa z(\epsilon - \overline{w'b'})]^{\frac{1}{3}}, & \text{if } \phi_m(\xi) = 1; \\ [\kappa z(\epsilon - 0.4\overline{w'b'})]^{\frac{1}{3}}, & \text{if } \phi_m(\xi) = 1 + 0.6\xi. \end{cases} \tag{8}$$

The stabilizing buoyancy production associated with melting ice is

$$\overline{w'b'} = gm' \left[\alpha \left((T_\infty - T_b) + \frac{L}{c_p} + \frac{c_I}{c_p}(T_b - T_I)\right) - \beta S_\infty\right], \tag{9}$$

where α and β are the thermal expansion and saline contraction coefficients (Appendix A). The 'far-field' ocean temperature and salinity are represented by T_∞ and S_∞. The variables $g = 9.81$ m s^{-2}, $c_p = 3974$ J kg^{-1} °C^{-1} and $L = 3.35 \times 10^5$ J kg^{-1} represent the gravity, specific heat capacity of seawater and latent heat of ice fusion, respectively. The velocity of the ocean in the direction normal to the ice-ocean interface is represented by m', and the melt rate of ice is $m = \rho m'/\rho_{ice}$, where ρ_{ice} is the density of ice. The m' is determined by the three-equation model, which links the local freezing relation and

the balance of heat and salt fluxes at the ice-ocean interface. The local freezing relation constrains the temperature T_b and salinity S_b at the ice-ocean interface:

$$T_b = aS_b + b + cP, \tag{10}$$

where $a = -0.0573°\mathrm{C}$, $b = 0.0832°\mathrm{C}$ and $c = -7.53 \times 10^{-8}°\mathrm{C\ Pa^{-1}}$, and P is the local hydrostatic pressure. The balances of heat and salt fluxes between the ice and ocean are

$$m'L + m'c_I(T_b - T_I) = c_p\gamma_T u_*(T_\infty - T_b) \quad \text{and} \tag{11}$$

$$m'S_b = \gamma_S u_*(S_\infty - S_b), \tag{12}$$

where $T_I = -25°\mathrm{C}$ and $c_I = 2009\mathrm{J\ kg^{-1}\ °C^{-1}}$ are the internal temperature and specific heat capacity of ice. The variables γ_T and γ_S are the non-dimensional exchange coefficients of the heat and salt transfer through the boundary layer, where these numbers are a function of the molecular Prandtl number (the ratio of viscosity to thermal diffusivity) and Schmidt number (the ratio of viscosity to saline diffusivity), respectively. According the formula by *Holland and Jenkins* [1999], we have assumed $\gamma_T = 1.27 \times 10^{-2}$ and $\gamma_S = 1.14 \times 10^{-4}$. The three equations (10) - (12), combined with (8) and (9), are solved simultaneously to compute the three unknowns m', T_b and S_b from given T_∞, S_∞ and ϵ. A procedure to solve the equations is outlined in Appendix B. The 'far-field' ocean temperature and salinity are combined to calculate the thermal driving:

$$T_* = T_\infty - (aS_\infty + b + cP). \tag{13}$$

5.2. Estimate of u_* and its effect on melt rate, m

The key to a consistent ice-shelf-ocean boundary layer parameterization lies in the choice of the friction velocity. Our measurement shows that average and maximum ϵ near the

ice base are 3×10^{-9} W kg^{-1} and 6.2×10^{-8} W kg^{-1}. The thermal driving beneath the ice shelf where ϵ are taken ($\sim$ 0.5 m below ice) is between 1.6 and 2.2 °C. From these observations near the ice base, our estimates of u_* are between 0.001 and 0.0035 m s^{-1} (Fig. 8a). Incorporating the effect of melting on the large-scale shear dU/dz by using $\phi_m(\xi) = 1 + 0.6\xi$ decrease 30% compared with $\phi_m(\xi) = 1$. This is consistent with the idea that the presence of stratification suppresses the turbulence, thereby reducing the friction velocity. Increasing u_* implies more heat is available to melt the ice, and the melt rate increases with increasing u_* (Fig. 8b). Based on observed ϵ and U_∞, we estimate the melt rate of this area to be between 10 and 33 m yr^{-1}.

5.3. Estimations of the Obukhov length scale, L_o

The Obukhov length, L_o, represents the height at which the buoyancy production of turbulence kinetic energy is equal to the shear production. Within L_o from the ice-ocean interface, the shear production dominates over the buoyancy production. The value of L_o can provide a practical measure of the deviation from statically neutral state with decreasing L_o corresponding to larger deviation from the neutral state. From the observed ϵ, L_o is at most a meter (Fig 8c).

In the absence of thermal driving T_*, the ice does not melt, thereby $L_o = \infty$ (Fig 9). L_0 decreases with increasing T_* due to more melting, which results in increasing buoyancy forcing. More mechanical energy is available for higher ϵ, increasing the shear production term, and therefore L_o increases with increasing ϵ. The presented analysis relies on the forms of $\phi_m(\xi)$, derived from the atmospheric surface layer. A key nature of the ice-shelf base is a reactive boundary and is not subjected to the wind forcing, unlike the surface

boundary layer of the ocean and the atmospheric surface layer. An empirical form of $\phi_m(\xi)$ beneath an ice shelf will help reduce the uncertainty of this analysis.

6. Conclusions

We have analyzed turbulence data collected by the AUV from PIG Ice Shelf cavity. In light of these observations, we estimated the friction velocity and melt rate from ϵ. Our main findings are as follows:

1. The highest $\epsilon = O(10^{-7})$ is observed when the AUV is the closest to the grounding line (2 km away from the southern part of the grounding line), where the outflow of meltwater occurs. Another region of high ϵ is found over the ridge where high density gradient is maintained by the baroclinic front of the modefied CDW and meltwater.

2. Our measurement shows that average ϵ and χ_T near the ice base are 3×10^{-9} W kg^{-1} and 2.3×10^{-6} °C^2 s^{-1}, respectively. From these measurements, we have estimated the friction velocity, assuming that the shear production term is balanced by the buoyancy flux from melting ice and ϵ. This assumption constrains the friction velocity and melt rate by ϵ. We have assumed two different forms of non-dimensional mean shear, $\phi_m(\xi) = 1$ (statically neutral boundary layer) and $\phi_m(\xi) = 1+0.6\xi$ (stably stratified boundary layer). Assuming the stably stratified boundary layer reduces the average friction velocity and melt rate from 0.0021 m s^{-1} to 0.0015 m s^{-1} and from 20 m yr^{-1} to 13 m yr^{-1} in the limited range of our observation.

3. The estimated Obukhov length scale from the friction velocity is at most 1 m with the average of 0.4 m, i.e., the production of turbulence kinetic energy by shear production is dominant only within a meter of the ice-ocean interface. Below the depth of Obukhov

length, stabilizing buoyancy flux from ice melting dominates the production of turbulence kinetic energy compared with shear production. This implies that estimating friction velocity for calculating basal melt rate from oceanic conditions below 1 m needs to consider the production of turbulence kinetic energy from ice melting.

Appendix A: Derivation of $\overline{w'b'}$

The buoyancy flux associated with melting of ice shelf ($\overline{w'b'}$) is related to the density deficit, $\Delta\rho$,

$$\overline{w'b'} = -gm'\Delta\rho, \quad \text{where} \quad \Delta\rho = -\alpha(T_\infty - T) + \beta(S_\infty - S). \tag{A1}$$

The variables T and S are temperature and salinity within the ice-ocean boundary layer,

$$T = T_b - \frac{\gamma_T u_*(T_\infty - T_b)}{m'} \quad \text{and} \quad S = S_b - \frac{\gamma_S u_*(S_\infty - S_b)}{m'}, \tag{A2}$$

where T_b and S_b are the temperature and salinity at the ice/ocean interface. The second terms $\frac{\gamma_T u_*(T_\infty - T_b)}{m'}$ and $\frac{\gamma_S u_*(S_\infty - S_b)}{m'}$ represent the oceanic contribution of temperature and salinity. We now rewrite (A2) using (11) and (12),

$$T = T_b - \frac{L}{c_p} - \frac{c_I}{c_p}(T_b - T_I) \quad \text{and} \quad S = 0. \tag{A3}$$

Substitutions of the above expressions into (A1) gives

$$\overline{w'b'} = gm' \left[\alpha \left(T_\infty - T_b + \frac{L}{c_p} + \frac{c_I}{c_p}(T_b - T_I) \right) - \beta S_\infty \right]. \tag{A4}$$

Appendix B: A procedure to solve the three-equation model in section 5

We will solve for 1) S_b then 2) m'.

B1. Solve for S_b

The quadratic equation for S_b is derived by combining (11) and (12):

$$AS_b^2 + BS_b + C = 0. \tag{B1}$$

The solution for S_b is

$$S_b = \frac{-B \pm \sqrt{B^2 - 4AC}}{2A}, \tag{B2}$$

where

$$A = a(c_p\gamma_T - \gamma_S c_I), \quad B = \gamma_S(S_\infty c_I a - L) - \gamma_S c_I(b + cP - T_I) + c_p\gamma_T(b + cP - T_\infty) \tag{B3}$$

and

$$C = \gamma_S S_\infty(L + c_I(b + cP - T_I)). \tag{B4}$$

The variables A, B and C do not contain any unknowns. Once the S_b is determined, T_b is computed by the freezing relationship (10).

B2. Solve for m'

We are now left to determine m' from solving (12). The expression for u_* in terms of m' is

$$u_* = \left[\kappa z\left(\epsilon - (1-\gamma)gm'\left[\alpha\left((T_\infty - T_b) + \frac{L}{c_p} + \frac{c_I}{c_p}(T_b - T_I)\right) - \beta S_\infty\right]\right)\right]^{\frac{1}{3}}. \tag{B5}$$

Substituting (B5) into (12) gives

$$(m'S_b)^3 = \gamma_S^3(S_\infty - S_b)^3\kappa z\left[\epsilon - (1-\gamma)gm'\left[\alpha\left((T_\infty - T_b) + \frac{L}{c_p} + \frac{c_I}{c_p}(T_b - T_I)\right) - \beta S_\infty\right]\right]. \tag{B6}$$

When the far-field salinity is equal to the salinity at the ice-ocean interface ($S_\infty = S_b$, implying $T_* = 0$), the ice does not melt ($m' = 0$). Rearranging the above equations results

in a cubic equation for m':

$$m'^3+\frac{\kappa z\gamma_S^3(S_\infty-S_b)^3}{S_b^3}(1-\gamma)gm'\left[\alpha\left((T_\infty-T_b)+\frac{L}{c_p}+\frac{c_I}{c_p}(T_b-T_I)\right)-\beta S_\infty\right]-\kappa z\epsilon\frac{\gamma_S^3(S_\infty-S_b)^3}{S_b^3}=0. \tag{B7}$$

The cubic equation is numerically solved to determine m' from given T_∞, S_∞ and ϵ.

Acknowledgments. The authors thank the captain and crews of Royal Research Ship James Clark Ross. This work was supported by funding from the UK Natural Environment Research Council's iSTAR Programme and NERC Grant Number XXXXXX.

References

Batchelor, G. K. (1959), Small-scale variation of convected quantities like temperature in turbulent fluid part 1. general discussion and the case of small conductivity, *Journal of Fluid Mechanics*, *5*(01), 113–133.

Businger, J. A., J. C. Wyngaard, Y. Izumi, and E. F. Bradley (1971), Flux-profile relationships in the atmospheric surface layer, *Journal of the Atmospheric Sciences*, *28*(2), 181–189.

De Rydt, J., P. R. Holland, P. Dutrieux, and A. Jenkins (2014), Geometric and oceanographic controls on melting beneath pine island glacier, *Journal of Geophysical Research: Oceans*, *119*(4), 2420–2438, doi:10.1002/2013JC009513.

Dutrieux, P., C. Stewart, A. Jenkins, K. W. Nicholls, H. F. J. Corr, E. Rignot, and K. Steffen (2014a), Basal terraces on melting ice shelves, *Geophysical Research Letters*, *41*(15), 2014GL060,618, doi:10.1002/2014GL060618.

Dutrieux, P., J. De Rydt, A. Jenkins, P. R. Holland, H. K. Ha, S. H. Lee, E. J. Steig, Q. Ding, E. P. Abrahamsen, and M. Schröder (2014b), Strong sensitivity of pine island

ice-shelf melting to climatic variability, *Science*, *343*(6167), 174–178.

Dyer, A. J. (1974), A review of flux-profile relationships, *Boundary-Layer Meteorology*, *7*(3), 363–372, doi:10.1007/BF00240838.

Favier, L., G. Durand, S. L. Cornford, G. H. Gudmundsson, O. Gagliardini, F. Gillet-Chaulet, T. Zwinger, A. J. Payne, and A. M. Le Brocq (2014), Retreat of pine island glacier controlled by marine ice-sheet instability, *Nature Clim. Change*, *4*(2), 117–121.

Gade, H. G. (1979), Melting of ice in sea water: A primitive model with application to the Antarctic ice shelf and icebergs, *J. Phys. Oceanogr.*, *9*, 189–198.

Greisman, P. (1979), On upwelling driven by the melt of ice shelves and tidewater glaciers, *Deep Sea Research Part A. Oceanographic Research Papers*, *26*(9), 1051 – 1065.

Halstead, M. (1943), A stability-term in the wind-gradient equation, *Eos, Transactions American Geophysical Union*, *24*(1), 204–208, doi:10.1029/TR024i001p00204.

Holland, D. M., and A. Jenkins (1999), Modeling thermodynamic ice–ocean interactions at the base of an ice shelf, *J. Phys. Oceanogr.*, *29*, 1787–1800.

Holland, D. M., and A. Jenkins (2001), Adaptation of an isopycnic coordinate ocean model for the study of circulation beneath ice shelves, *Monthly Weather Review*, *129*, 1905–1927.

Holland, P. R., A. Jenkins, and D. M. Holland (2008), The response of ice shelf basal melting to variations in ocean temperature, *Journal of Climate*, *21*(11), 2558–2572, doi:10.1175/2007JCLI1909.1.

Jacobs, S. S., A. L. Gordon, and J. L. A. Jr (1979), Circulation and melting beneath the Ross Ice Shelf, *Science.*, *203*, 441–443.

Jacobs, S. S., H. H. Helmer, and A. Jenkins (1996), Antarctic ice sheet melting in the southeast Pacific, *Geophys. Res. Lett.*, *23*, 957–960.

Jacobs, S. S., A. Jenkins, C. F. Giulivi, and P. Dutrieux (2011), Stronger ocean circulation and increased melting under pine island glacier ice shelf, *Nature. Geoscience.*, *4*, 519–523.

Jenkins, A., P. Dutrieux, S. Jacobs, S. McPhail, J. Perrett, A. Webb, and D. White (2010), Observations beneath Pine Island Glacier in West Antarctica and implications for its retreat, *Nature. Geoscience.*, *3*, 468–472.

Joughin, I., E. Rignot, C. E. Rosanova, B. K. Lucchitta, and J. Bohlander (2003), Timing of recent accelerations of pine island glacier, antarctica, *Geophysical Research Letters*, *30*(13), n/a–n/a, doi:10.1029/2003GL017609.

Joughin, I., B. E. Smith, and B. Medley (2014), Marine ice sheet collapse potentially under way for the thwaites glacier basin, west antarctica, *Science*, *344*(6185), 735–738.

Kimura, S., K. W. Nicholls, and E. Venables (2015), Estimation of ice shelf melt rate in the presence of a thermohaline staircase, *Journal of Physical Oceanography*, *45*(1), 133–148, doi:10.1175/JPO-D-14-0106.1.

Levine, E. R., and R. G. Lueck (1999), Turbulence measurement from an autonomous underwater vehicle, *J. Atmos. Oceanic Technol.*, *16*, 1533–1544.

Little, C. M., A. Gnanadesikan, and M. Oppenheimer (2009), How ice shelf morphology controls basal melting, *Journal of Geophysical Research: Oceans*, *114*(C12), C12,007, doi:10.1029/2008JC005197.

Losch, M. (2008), Modeling ice shelf cavities in a z-coordinate ocean general circulation model, *J. Geophys. Res.*, *113*, C08,043.

Monin, A., and A. Obukhov (1954), Basic laws of turbulent mixing in the surface layer of the atmosphere, *Tr. Akad. Nauk SSSR Geophiz. Inst*, *24*(151), 163–187.

Nicholls, K. W., and A. Jenkins (1993), Temperature and salinity beneath Ronne ice shelf, Antarctica, *J. Geophys. Res.*, *98(C12)*, 22,553–22,568.

Osborn, T., and W. Crawford (1980), *An Airfoil Probe for Measuring Turbulent Velocity Fluctuations in Water*, vol. Dobson, F. and Hasse, L. and Davis, R., Springer US.

Pritchard, H. D., R. J. Arthern, D. G. Vaughan, and L. A. Edwards (2009), Extensive dynamic thinning on the margins of the greenland and Antarctic ice sheets, *Nature.*, *461*, 971–975.

Rignot, E., J. Mouginot, M. Morlighem, H. Seroussi, and B. Scheuchl (2014), Widespread, rapid grounding line retreat of pine island, thwaites, smith, and kohler glaciers, west antarctica, from 1992 to 2011, *Geophysical Research Letters*, *41*(10), 3502–3509, doi: 10.1002/2014GL060140.

Rudnick, D. L., T. J. Boyd, R. E. Brainard, G. S. Carter, G. D. Egbert, M. C. Gregg, P. E. Holloway, J. M. Klymak, E. Kunze, C. M. Lee, M. D. Levine, D. S. Luther, J. P. Martin, M. A. Merrifield, J. N. Moum, J. D. Nash, R. Pinkel, L. Rainville, and T. B. Sanford (2003), From tides to mixing along the hawaiian ridge, *Science*, *301*(5631), 355–357.

Schoof, C. (2007), Ice sheet grounding line dynamics: Steady states, stability, and hysteresis, *J. Geophys. Res.*, *112*, F03S28.

Sheen, K. L., A. C. Naveira Garabato, J. A. Brearley, M. P. Meredith, K. L. Polzin, D. A. Smeed, A. Forryan, B. A. King, J.-B. Sallee, L. St. Laurent, A. M. Thurnherr, J. M. Toole, S. N. Waterman, and A. J. Watson (2014), Eddy-induced variability in southern

ocean abyssal mixing on climatic timescales, *Nature Geosci*, *7*(8), 577–582.

Shepherd, A., D. J. Wingham, J. A. D. Mansley, and H. F. J. Corr (2001), Inland thinning of pine island glacier, west antarctica, *Science*, *291*(5505), 862–864, doi: 10.1126/science.291.5505.862.

Soulsby, R. (1983), The bottom boundary layer of shelf seas, *Physical Oceanography of Coastal and Shelf Seas*, *B. John Ed., Elsevier Oceanogr. Ser. 35*, 189–266.

Stanton, T. P., W. J. Shaw, M. Truffer, H. F. J. Corr, L. E. Peters, K. L. Riverman, R. Bindschadler, D. M. Holland, and S. Anandakrishnan (2013), Channelized ice melting in the ocean boundary layer beneath pine island glacier, antarctica, *Science*, *341*, 1326–1329.

Tennekes, H., and J. L. Lumley (1972), *A First Course in Turbulence*, MIT Press, Cambridge, Mass.

Vaughan, D. G., H. F. J. Corr, R. A. Bindschadler, P. Dutrieux, G. H. Gudmundsson, A. Jenkins, T. Newman, P. Vornberger, and D. J. Wingham (2012), Subglacial melt channels and fracture in the floating part of pine island glacier, antarctica, *Journal of Geophysical Research: Earth Surface*, *117*(F3), n/a–n/a, doi:10.1029/2012JF002360.

References

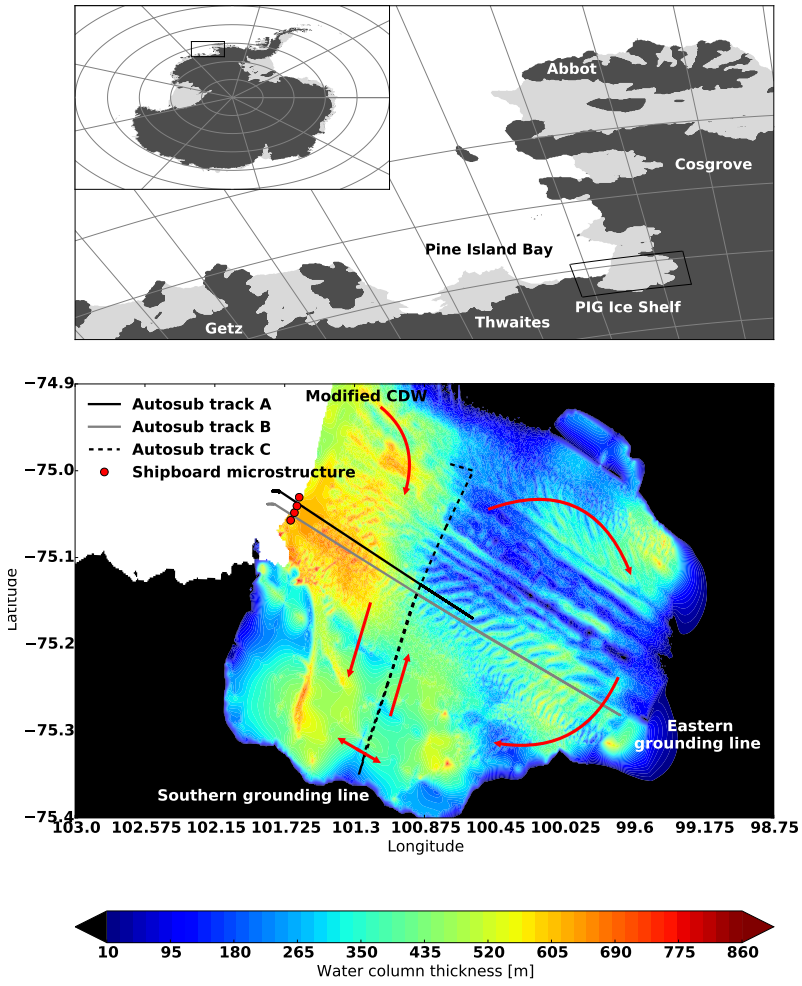

Figure 1. Maps showing the Amundsen Sea and Pine Island Bay. Three Autosub mission tracks beneath PIG Ice Shelf and locations of the shipboard microstructure measurements. The water column thickness beneath the ice shelf is colorcoded. The water column thickness is defined as the difference between the sea bed depth and ice draft derived from upward looking ADCP mounted on the AUV. Red arrows indicate a schematic representation of CDW inflow into the ice shelf cavity and its circulation.

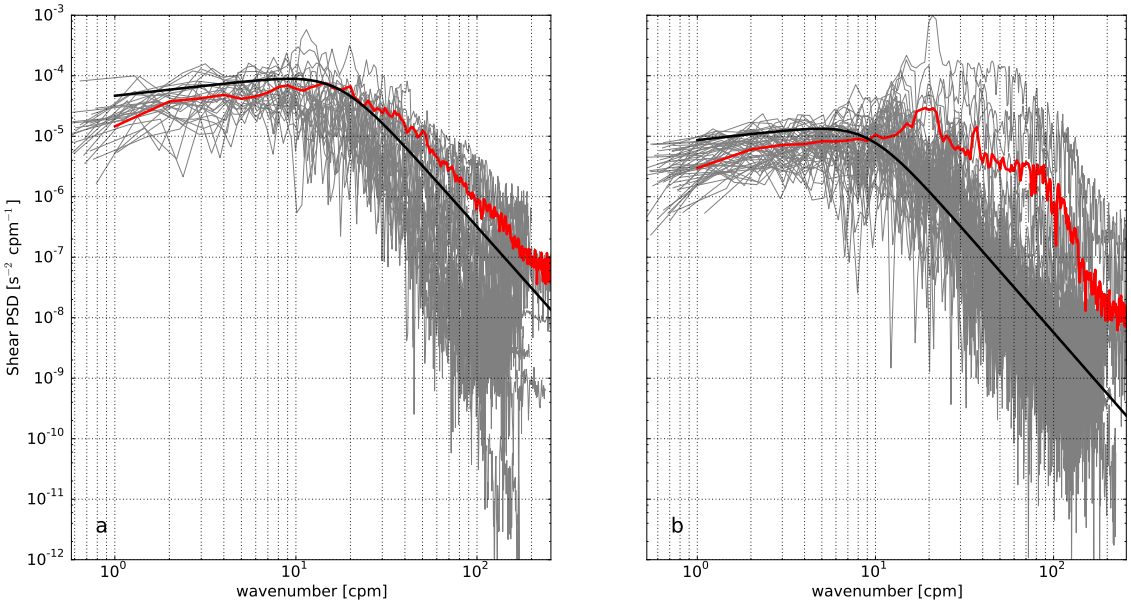

Figure 2. Power spectra for (a) $\epsilon \approx 1.3 \times 10^{-8}$ W kg^{-1} (18 spectra) and (b) $\epsilon \approx 1 \times 10^{-9}$ W kg^{-1} (41 spectra). The individual spectra are shown in gray and the mean spectra are shown in red. The dark curves indicate the corresponding Nasmyth universal spectra for each ϵ

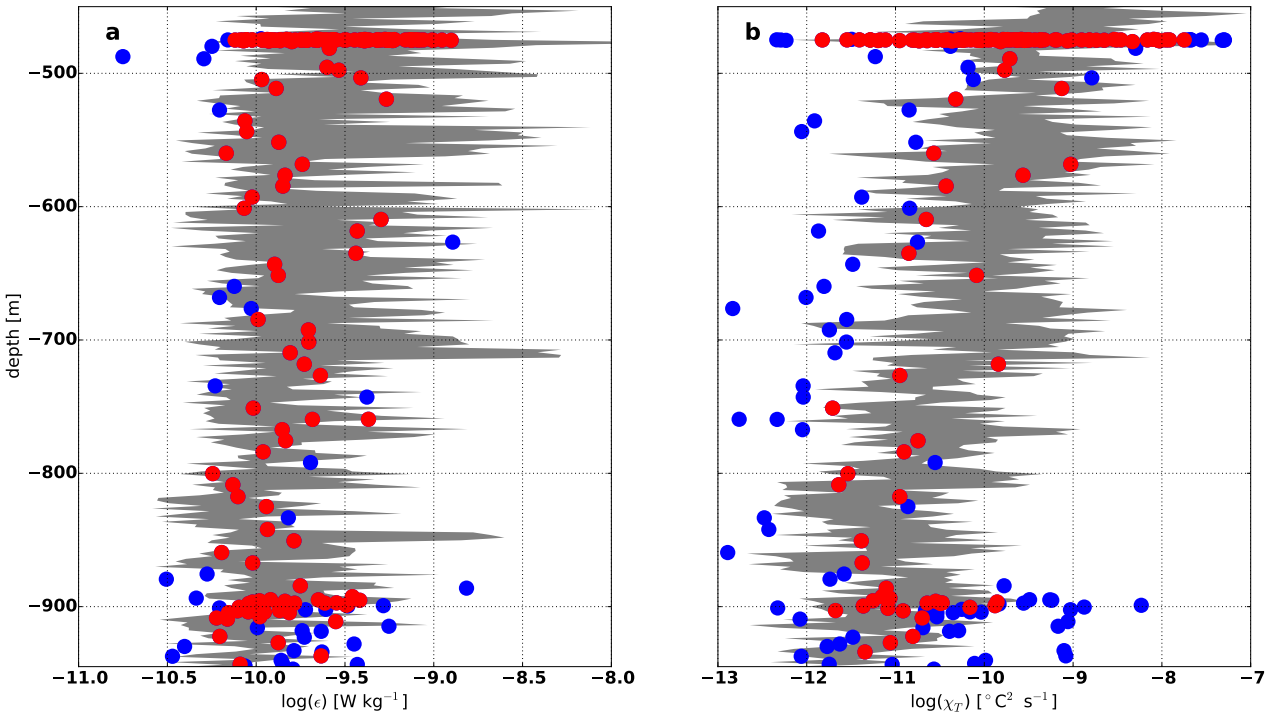

Figure 3. Comparison of the shipboard and AUV microstructure measurements (a) ϵ and (b) χ_T. The shaded region shows the range of ϵ and χ_T profiles from 4 shipboard measurements within 4 km of the AUV track. The location of 4 shipboard measurements are indicated in Fig. 1. Red dots indicate the AUV measurements that lie within the shaded region, whereas the measurements outside of the shaded region are colorcoded in blue.

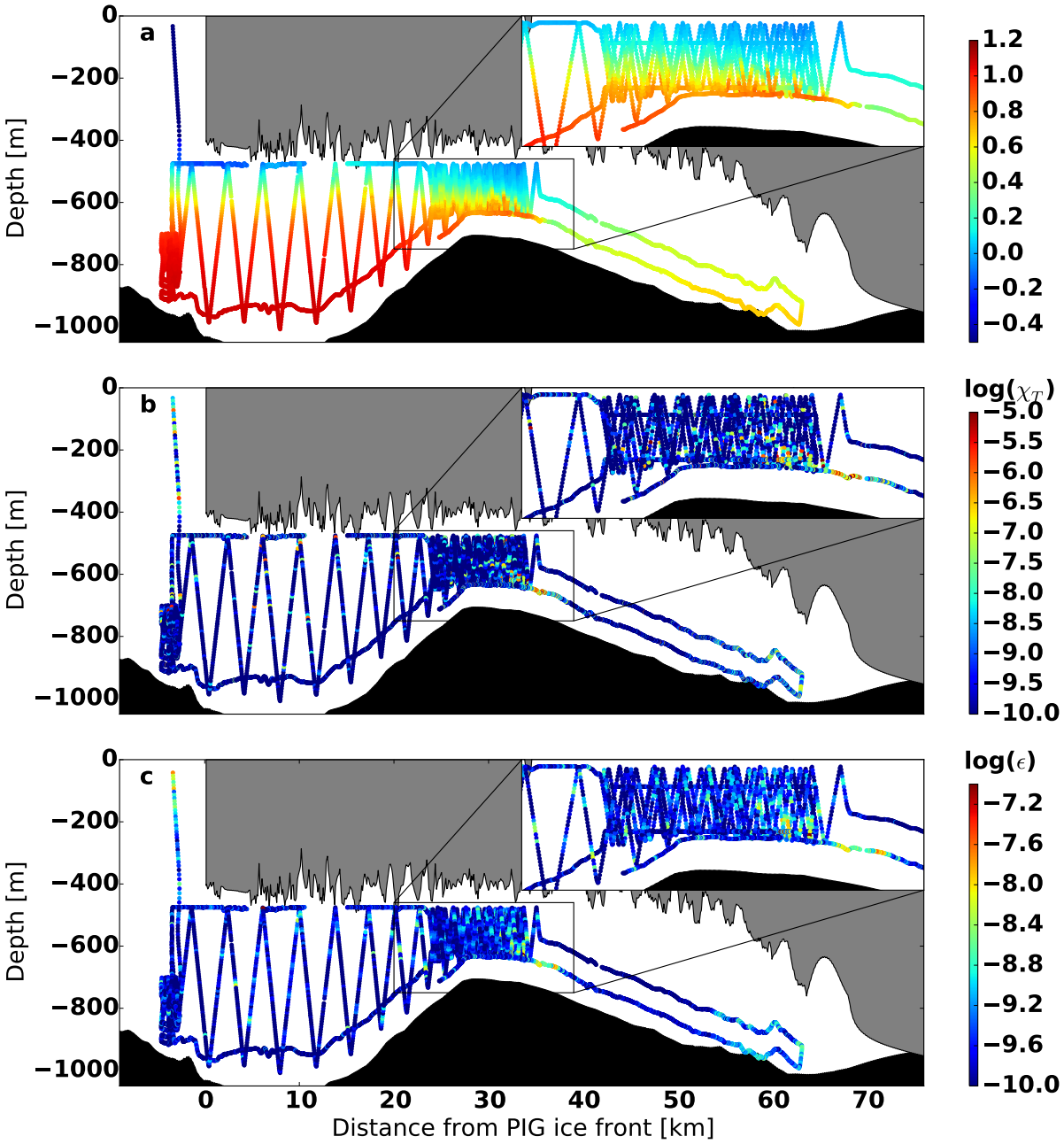

Figure 4. (a) Potential temperature, (b) χ_T, (c) ϵ from the AUV track A and B. The ice draft and seabed depth are derived from the 2009 ADCP range data along track A.

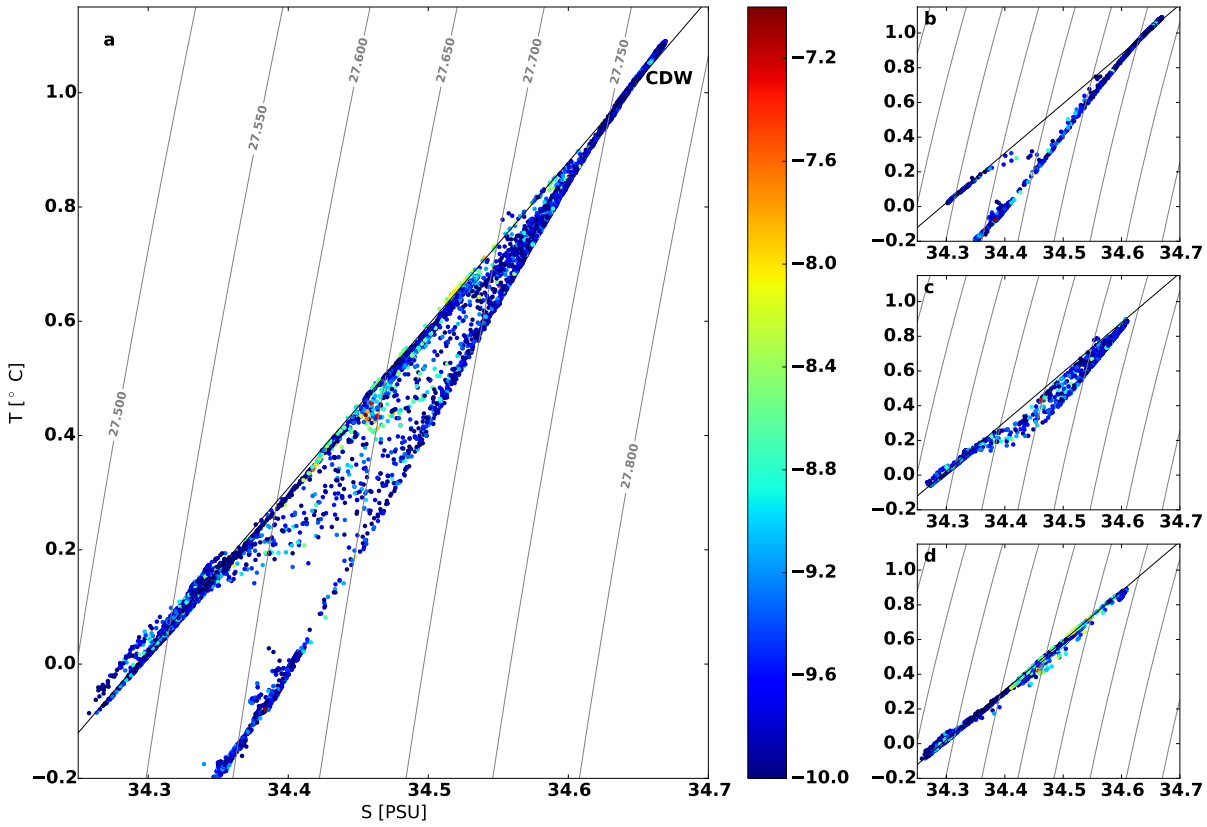

Figure 5. (a) T-S diagram from all the AUV observations in 2014. The color indicates $\log(\epsilon)$, and the solid line is a meltwater mixing line. T-S diagram of selected regions (b) seaward side of the cavity between 0 and 20 km away from the ice front, (c) crest of the ridge, between 28 and 32 km away from the ice front, (d) inshore side of the ridge, >32 km away from the ice front.

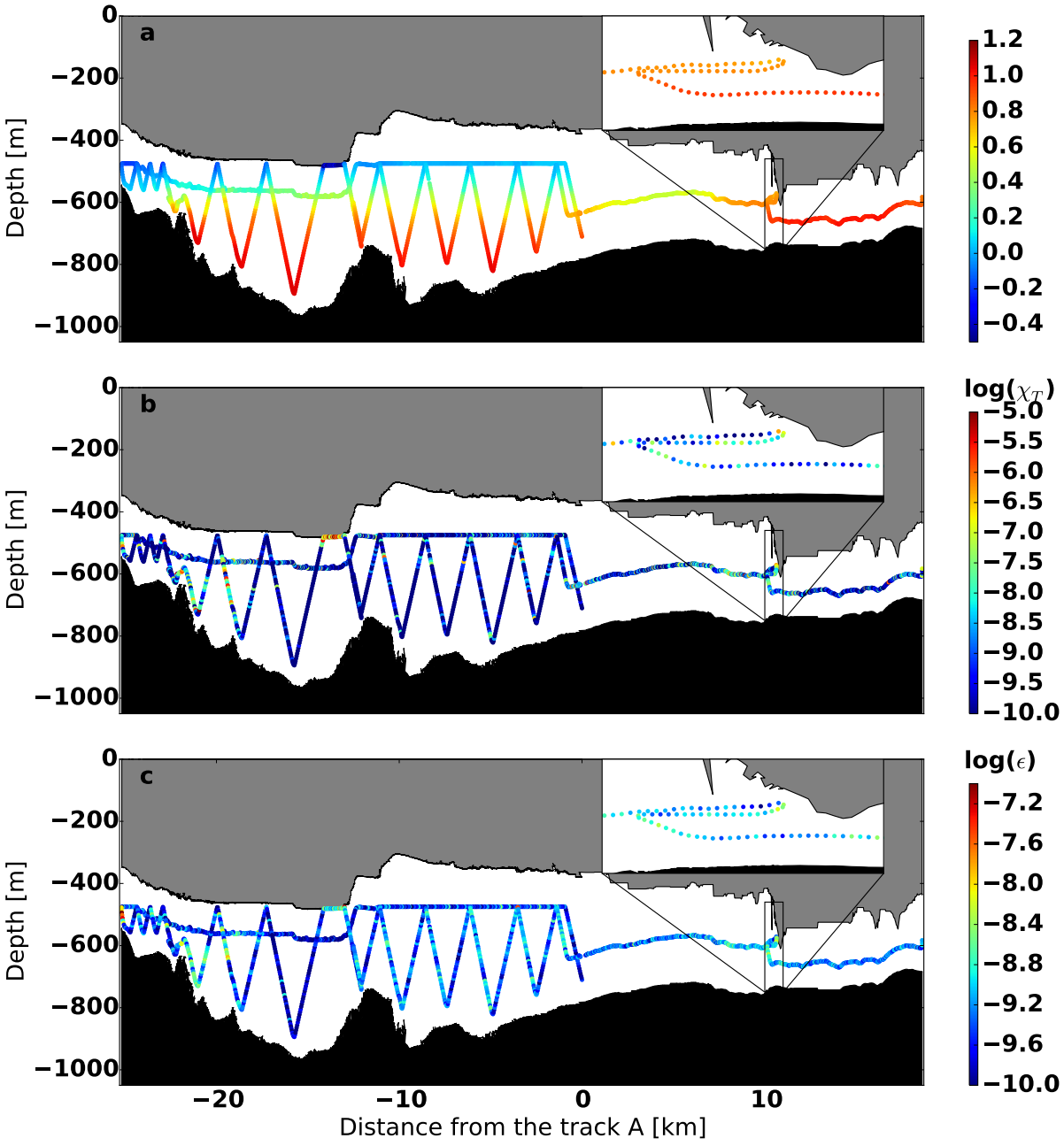

Figure 6. (a) Potential temperature, (b) χ_T, (c) ϵ from the track C. The horizontal axes indicate the distance from the intersection of the tracks A and C (see Fig 1), and the vertical axes is the depth. The ice draft and bed depth are derived from the AUV's sonar device.

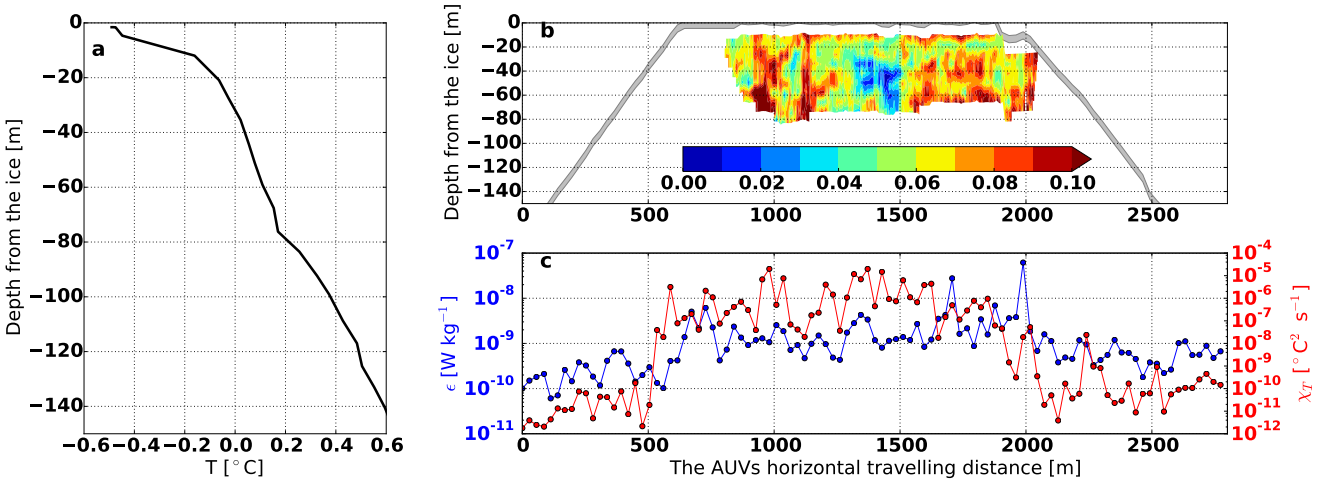

Figure 7. Oceanic conditions in the vicinity of the ice, the segment of transect between -15 and -12 km in Fig 6. (a) The solid dark line indicates the temperature profiles during the ascend cast. (b) The water speed, m s^{-1}, derived from the ADCP is colorcoded, during up, horizontal and down casts. The shaded region indicate the AUV track. During the horizontal cast, the AUV traveled within 1 m of the ice shelf. (c) ϵ (blue) and χ_T (red) measurements over this section of the AUV track.

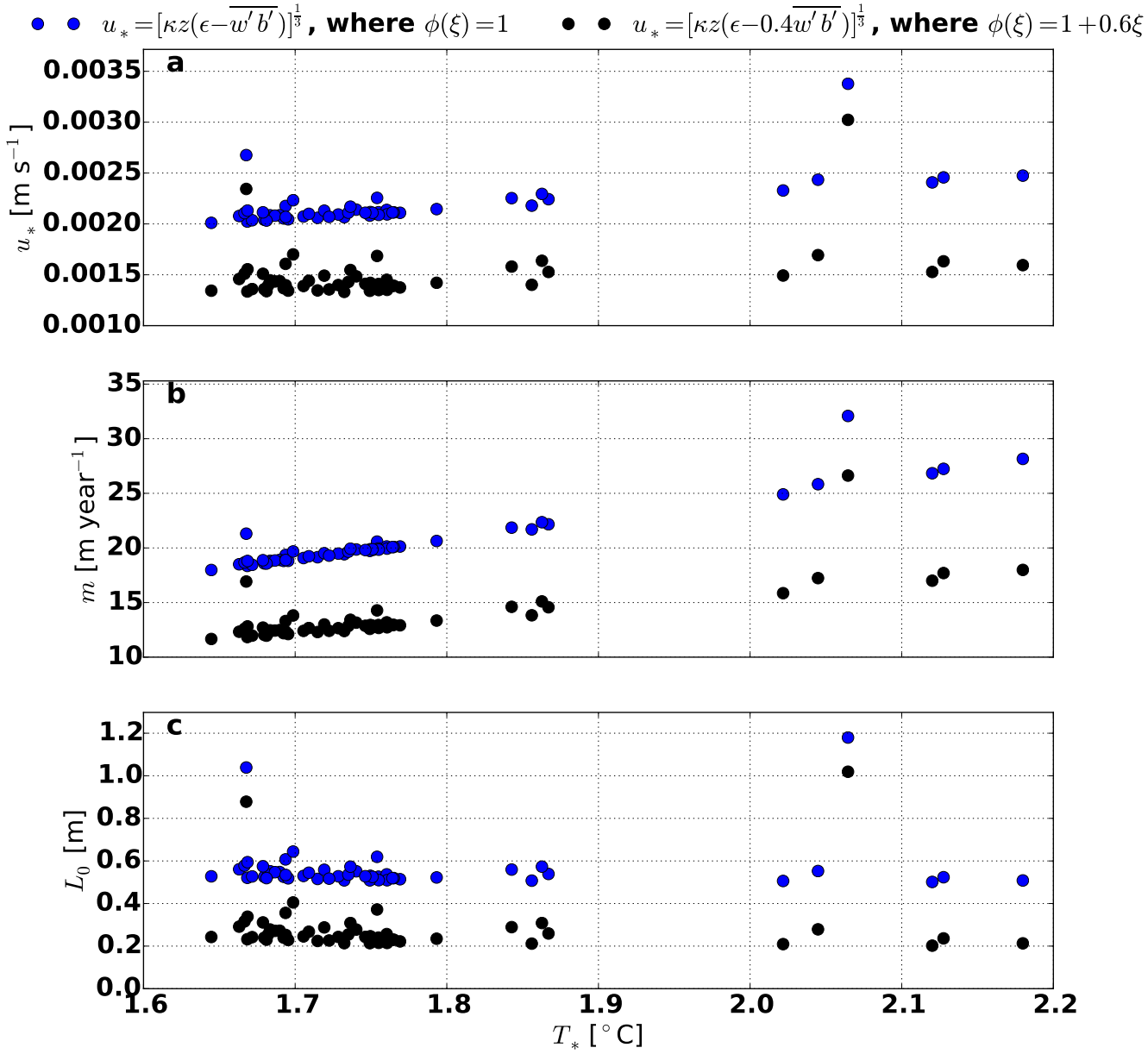

Figure 8. Comparison of the friction velocity (a), melt rate (b) and Obukhov length (c) estimated from our observations.

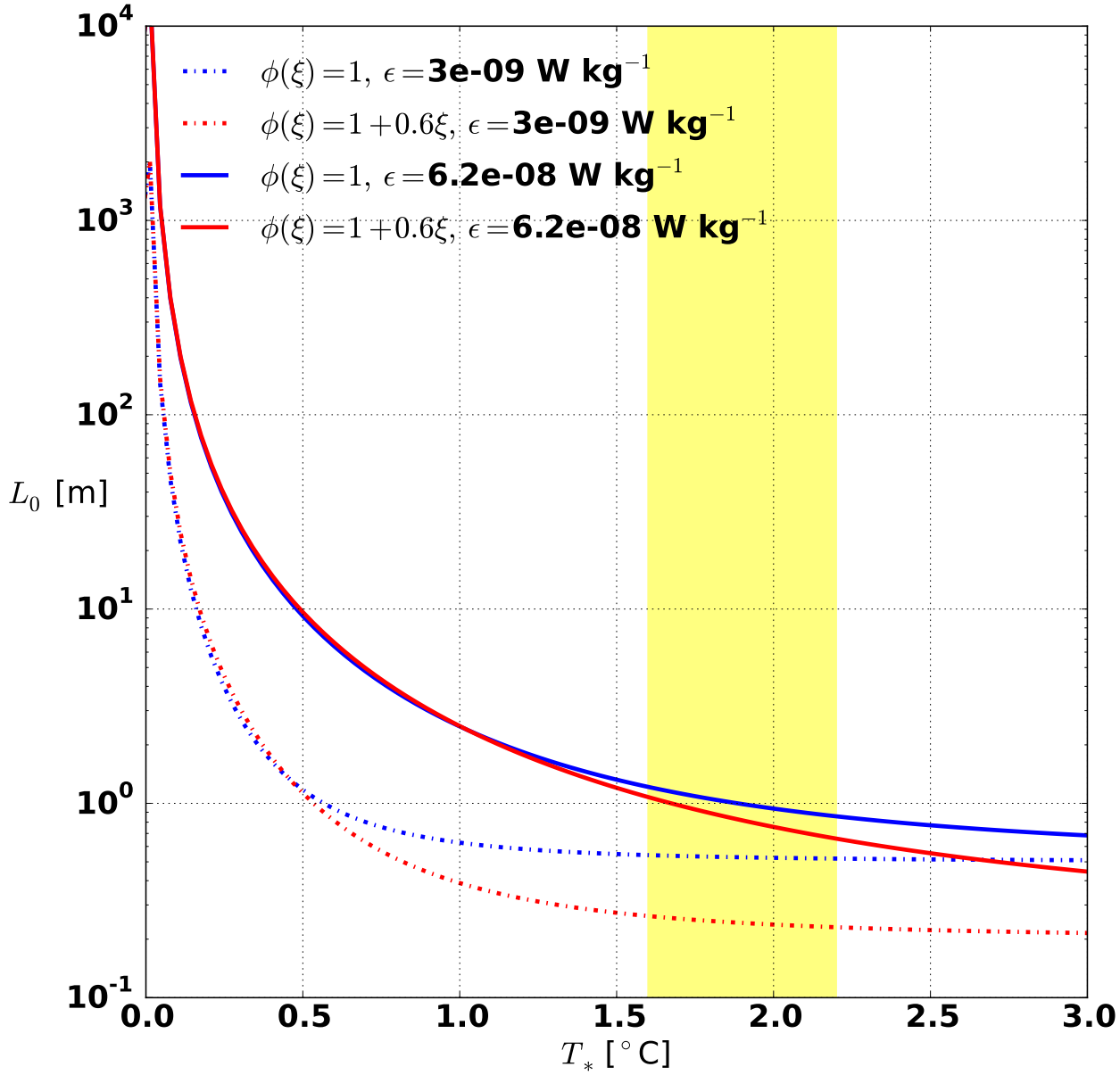

Figure 9. Estimation of the Obukhov length, L_o with respect to the thermal driving T_* for different forms of $\phi_m(\xi)$ and values of ϵ. The yellow shaded region indicates the observed range of thermal driving from the AUV ($\sim$ 0.5 m away from the ice). Our measurement shows that average and maximum ϵ near the ice base are 3×10^{-9} W kg^{-1} and 6.2×10^{-8} W kg^{-1}.